Nano Today 69 (2026) 103061

Contents lists available at ScienceDirect

Nano Today

journal homepage: www.elsevier.com/locate/nanotoday

BBB-penetrating biomimetic nanoparticles orchestrate STING activation and metabolic immunomodulation for potent glioma immunotherapy

Yang Tian [a,b,c,d], Chang Na [a,b,c,d], Qi Sun [a,b,c,d], Chunyu Zhao [a,b,c,d], Wentao Zhang [a,b,c,d], Yan Su [c,e], Dong Mei [c,f], Yitong Liu [d,g], Ran Huo [a,b,c,d], Siyu Liu [a,b,c,d], Yadong Xing [a,b,c,d], Jingyi Ye [a,b,c,d], Yingdong Ma [a,b,c,d], Shuxin Luo [a,b,c,d], Muhan Zhang [a,b,c,d], Yaoqi Wang [a,b,c,d,*], Shuang Zhang [a,b,c,d,*], Chunying Cui [a,b,c,d,*]

[a] School of Pharmaceutical Sciences, Capital Medical University, Beijing, China
[b] Beijing Area Major Laboratory of Peptide and Small Molecular Drugs, Beijing Laboratory of Biomedical Materials, Engineering Research Center of Endogenous Prophylactic of Ministry of Education of China, Beijing, China
[c] Laboratory for Clinical Medicine, Capital Medical University, Beijing, China
[d] Clinical Basic Cooperation Platform Cultivation Project, Capital Medical University, Beijing, China
[e] Medical Oncology Department, Pediatric Oncology Center, Beijing Children's Hospital, Capital Medical University, National Center for Children's Health, Beijing, China
[f] Department of Pharmacy, Beijing Children's Hospital, Capital Medical University, National Center for Children's Health, Beijing, China
[g] Laboratory of Tissue Regeneration and Immunology and Department of Periodontics, Beijing Key Laboratory of Tooth Regeneration and Function Reconstruction, School of Stomatology, Capital Medical University, Beijing, China

ARTICLE INFO

Keywords:
Biomimetic nanoparticles
Synergistic immunotherapy
STING pathway
Blood-brain barrier
Glioma

ABSTRACT

Immunotherapy for glioma is an attractive strategy yet faces significant barriers: (i) inefficient delivery across the blood-brain barrier (BBB), and (ii) a profoundly immunosuppressive microenvironment. To address these constraints, we engineered a biomimetic nanocarrier, where EGCG/Zn core loaded MSA-2 and siRNA-SLC43A2 was coated with glioma cell membrane-liposome fusions. Incorporation of an Angiopep-2 (Ang-2) targeting peptide was further intended to facilitate BBB transcytosis via LRP1-mediated transport. Leveraging its excellent immune activation capability and targeting specificity, this nanocarrier successfully traversed the BBB and delivered therapeutic agents precisely into glioma cells. MSA-2 activated STING pathway to trigger innate immune response and induce the $CD8^+$ T cells recruiting. Complementarily, siRNA targeting SLC43A2 reversed methionine depletion and alleviated $CD8^+$ T cell exhaustion and apoptosis by downregulating the methionine transporter in tumor cells. These two mechanisms synergistically enhanced anti-glioma immunotherapy by initiating the anti-tumor immune response and augmenting its therapeutic efficacy, respectively. This synergistic immunotherapy provides a promising novel strategy to overcome the challenges of glioma immunotherapy.

Introduction

Immunotherapy has demonstrated remarkable success in the treatment of various cancers; however, progress in glioma has remained limited to date [1,2]. Two major obstacles continue to constrain immunotherapeutic efficacy. First, despite partially disruption in high-grade diseases, the blood-brain/blood-tumor barrier (BBB), still impedes the penetration of many therapeutic agents and the trafficking of immune cells [3]. Second, gliomas are typical "cold tumors" characterized by a profoundly immunosuppressive environment: a multitude of immunosuppressive cells and immunosuppressive cytokines that impair immune cell function and survival [4]. Aberrant metabolic reprogramming competitively depletes critical nutrients and generates toxic metabolites, further suppressing anti-tumor immune responses [5,6]. Effective immunotherapeutic strategies for glioma must address these two fundamental barriers: efficient drug delivery and reversal of

* Correspondence to: Department of Pharmaceutics, School of Pharmaceutical Sciences, Capital Medical University, No. 10 Youanmenwai Street, Fengtai, Beijing 100069, China.
E-mail addresses: wangyaoqi@ccmu.edu.cn (Y. Wang), zshuang@ccmu.edu.cn (S. Zhang), ccy@ccmu.edu.cn (C. Cui).

https://doi.org/10.1016/j.nantod.2026.103061
Received 2 February 2026; Received in revised form 25 March 2026; Accepted 19 April 2026
Available online 6 May 2026
1748-0132/

immunosuppressive microenvironment.

MSA-2, an orally bioavailable, non-nucleotide agonist of the cGAS-STING pathway, can activate innate immune response and induce the production of type I interferons (IFN-β), thereby converting "cold" immunosuppressive tumors into "hot" immunologically responsive ones [7,8]. However, MSA-2 monotherapy faces certain risks in glioma: the negative charge and high molecular polarity conferred by its carboxylic acid group may limit its penetration across the BBB [9]. More importantly, the innate immune response induced by MSA-2 may be insufficient to activate and sustain an adequate number of functionally competent cytotoxic T cells within the immunosuppressive microenvironment, leading to an abortive immune response and limited therapeutic efficacy [10,11].

Based on this need for therapeutic potentiation, we turned to the emerging field of tumor immunometabolism. Recent studies have untangled that elevated SLC43A2 expression in tumor cells can competitively sequester methionine from the microenvironment, reducing methionine availability to T cells and perturbing S-adenosylmethionine (SAM)-dependent histone methylation programs. This directly suppresses T cell function at the epigenetic level, driving them into an exhausted state [12–14]. As a powerful tool for precise gene silencing, small interfering RNA (siRNA) exhibits great potential in targeted modulation of tumor metabolism and remodeling the immune microenvironment, providing a crucial technical pathway for developing novel combination immunotherapies [15]. Building on this, we employed siRNA to specifically knock down SLC43A2, aiming to relieve the metabolic constraints on T cells, reverse their functional exhaustion, and thereby reinforcing the functionally competent effector T cells in the tumor microenvironment.

Notably, recent studies have revealed that SLC43A2 not only directly influences T cell function by regulating methionine metabolism but also indirectly modulates the activation efficiency of the STING pathway. Given that methionine metabolism governs the biosynthesis of SAM, reduced intracellular SAM levels impair the carboxymethylation and maturation of nuclear lamins [16],while also disrupting DNA methylation [17]. These alterations collectively trigger the release of cytoplasmic chromatin fragments and subsequent activation of the STING pathway. These findings establish a direct functional crosstalk between SLC43A2 and the STING pathway, providing a profound theoretical foundation for designing synergistic therapeutic strategies co-targeting SLC43A2 and STING pathway.

Based on this rationale, we conceived a novel "synergistic immune initiation and potentiation" strategy, where MSA-2 serve as an immune activator to initiate the primary innate immune response, while siSLC43A2 functions as an immunometabolic modulator to relieve T cell functional suppression. This strategy aims to sponsor a multi-pronged synergistic assault on the immunosuppressive glioma microenvironment, eliciting a robust and durable anti-tumor immune response. However, the core technical bottleneck for realizing this strategy lies in how to co-deliver two agents with vastly different physicochemical properties (the hydrophobic small molecule MSA-2 and the hydrophilic macromolecule siRNA) to across the BBB and into brain tumors in a co-localized, efficient, and targeted manner.

To address this co-delivery challenge and remodel the tumor immunosuppressive environment of glioma, we meticulously designed and constructed a novel biomimetic nano-delivery platform:

1. Core (EGCG–Zn nanoparticles for dual loading)

   A stable nanoscale core was formed via the self-assembly of epigallocatechin gallate (EGCG) and zinc ions, forming a metal–polyphenol/coordination network with high structural tunability and payload compatibility. This core encapsulates the hydrophobic MSA-2 through π-π stacking interactions, while simultaneously achieving siRNA loading through efficient complexation between EGCG/Zn^{2+} and the negatively charged siSLC43A2, enabling co-encapsulation of both agents in a single nanostructure.

2. Shell (hybrid biomimetic membrane–liposome coating for targeting)

To endow the nanoparticle with active targeting capabilities, a hybrid biomimetic shell was constructed via membrane fusion technology, utilizing glioma cell membranes and Angiopep-2 (Ang-2) peptide-modified liposomes. Cell-membrane camouflage is widely recognized to confer homotypic (self-recognition) targeting and immune evasion, improving tumor accumulation. The incorporation of the Ang-2 peptide is designed to enhance BBB traversal and brain-targeted delivery, while the liposomal structure provides excellent biocompatibility and stability.

The schematic illustration of the construction process and action mechanism of the biomimetic nano-delivery platform is shown in Fig. 1. We hypothesize that this biomimetic nano-delivery platform can efficiently traverse the BBB and be targeted to accumulate in glioma regions. Within the tumor microenvironment, the release of MSA-2 and siSLC43A2 will enable a dual intervention on the immunosuppressive milieu: MSA-2-driven STING activation initiates innate immunity to recruit immune cells, while siSLC43A2 remodeling the metabolic microenvironment to rescue T cell function. This is anticipated to ultimately establish a powerful positive feedback loop of anti-tumor immunity, thereby efficiently inhibiting tumor progression. This study not only provides a promising new paradigm for synergistic intervention in glioma immunotherapy, but also offers innovative concepts and a technical foundation for the design of brain-targeted nanocarriers capable of co-delivering drugs with disparate properties.

Results

Preparation and Physicochemical characterization of Bionic Nanoparticle Delivery System

The EZ/M nanoparticles were fabricated through the self-assembly of epigallocatechin gallate (EGCG), dopamine, and zinc ions with the involvement of MSA-2. EZ/MS was then prepared by incubating EZ/M with siSLC43A2 at room temperature for 4 h. Unbound MSA-2 and siSLC43A2 were removed by ultrafiltration. The concentration of unbound MSA-2 was determined by high-performance liquid chromatography (HPLC). For Cy5-labeled siSLC43A2, the concentrations of total and free nucleic acids were quantified by via fluorescence intensity detection. Encapsulation efficiency was calculated as follows: EE (%) = [(Total concentration − Free concentration) / Total concentration] × 100%. The encapsulation efficiency of MSA-2 was (48.00 ± 0.02) %, while that of siSLC43A2 was (97.36 ± 1.9) %, respectively. To prepare AL-EZ/MS, the Ang-2 peptide-modified liposomes were employed for the encapsulation of EZ/MS. Finally, ACM-EZ/MS was prepared by fusing the Ang-2 peptide-modified liposomes with cell membranes through sonication. Other formulations were synchronously prepared as controls. The full names and corresponding abbreviations of all formulations are summarized in Table S1.

The physicochemical characterizations of ACM-EZ/MS nanoparticles were thoroughly evaluated. The stepwise size increase shown in Fig. 2A is attributed to the sequential encapsulation of liposomes and cell membranes. In Fig. 2B, siSLC43A2, as a large negatively charged molecular, partially shielded the influence of the original nanoparticle's negative charge on the environment, resulting in a decrease in the negative zeta potential. Subsequent coating with positively charged lipids resulted in a reversal of the zeta potential to a positive value. Further fusion with the negatively charged cell membrane then reduced the overall positive potential. The transmission electron microscopy (TEM) images (Fig. 2C) demonstrate a well-defined core-shell structure for ACM-EZ/MS, indicating the successful encapsulation of EZ/MS within the cell membrane-liposome fused complex (ACM). In the TEM-energy dispersive spectroscopy (TEM-EDS) mapping (Fig. 2D), the aggregation of Carbon elements, Oxygen elements, and Zinc elements confirms the formation of EZ nanoparticle. Additionally, the presence of

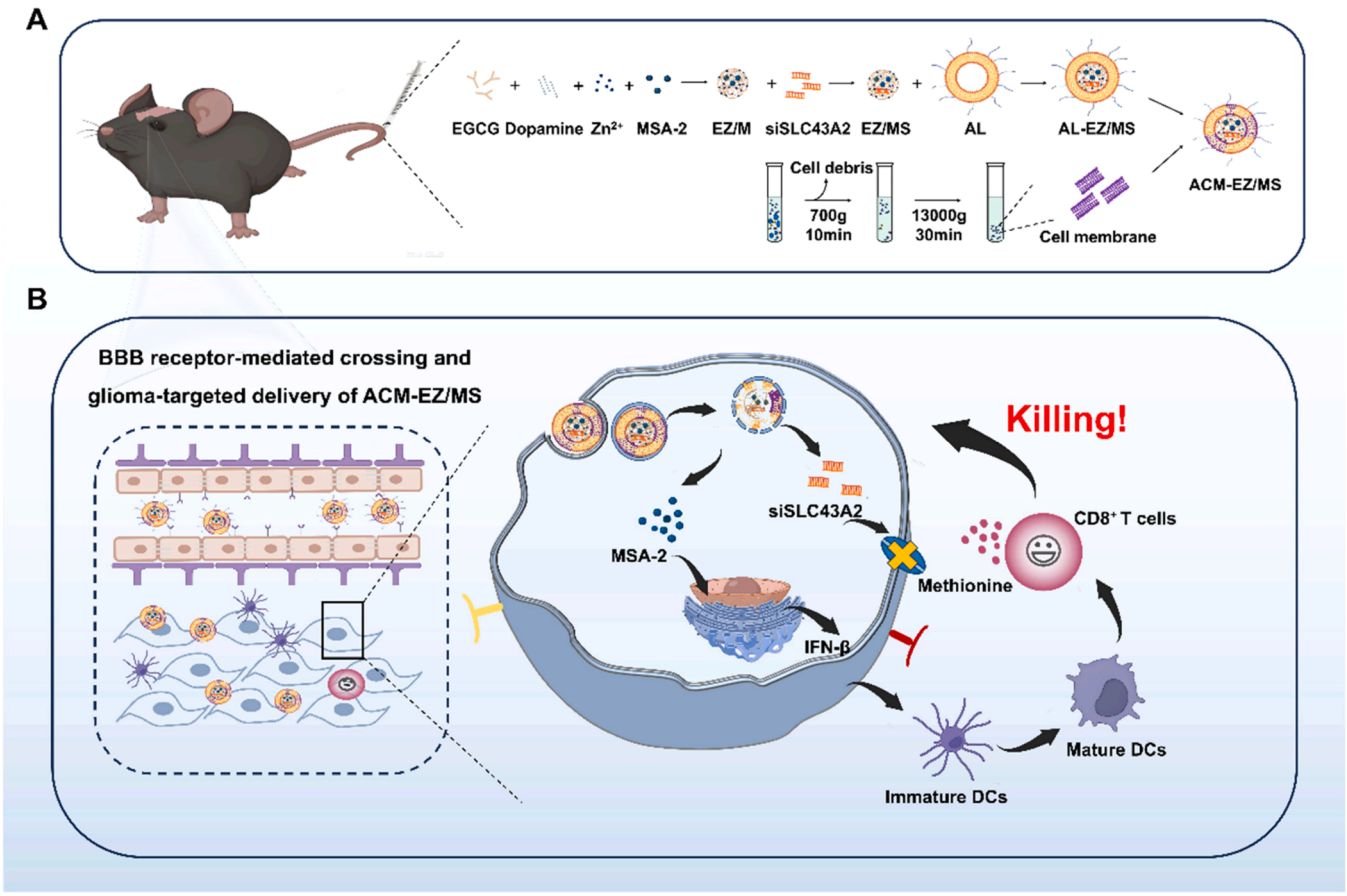

Fig. 1. (A) Schematic illustration of ACM-EZ/MS nano-delivery system construction. (B) Schematic Diagram of ACM-EZ/MS Mechanism: Crossing BBB and Potentiating Immune Responses in Glioma Cells After Intravenous Administration. Some graphical elements in this figure were adapted from BioRender with permission for publication. (EGCG, Epigallocatechin gallate; EZ/M, EGCG-Zn nanoparticles encapsulating MSA-2; EM/MS, EGCG-Zn nanoparticles encapsulating MSA-2 and siSLC43A2; AL, Angiopep-2 peptide-modified liposomes; AL-EZ/MS, EZ/MS-encapsulated liposomes modified with Angiopep-2 peptide; ACM-EZ/MS, Fusion hybrids of Angiopep-2 peptide-modified liposomes encapsulating EZ/MS and cell membranes; BBB, Blood-Brain Barrier; DCs, dendritic cells).

phosphorus elements (from siSLC43A2) and sulfur elements (from MSA-2) demonstrates the successful encapsulation of siSLC43A2 and MSA-2 within the EGCG-Zn nanoparticles. Fig. 2E visually demonstrates the co-localization of DiI-labeled liposomes and DiO-labeled cell membranes. The fluorescence spectrum before fusion shows a peak for the acceptor dye DiI around 565 nm, while after fusion, a peak for the donor dye DiO appears around 501 nm (Figure S1A). This indicates the successful insertion of liposomes into the cell membrane structure, which weakened the fluorescence resonance energy transfer (FRET) effect between the two dyes.

To investigate whether the nanoparticles could efficiently disassemble within tumor cells, EGCG release from the nanoparticles under acidic and neutral pH conditions (Figure S1B) was monitored. Under neutral conditions (pH 7.4), the cumulative release of EGCG did not exceed 30% within 48 h. A slight decline was observed after prolonged incubation, which was attributed to the instability and partial oxidation of EGCG in neutral aqueous environment [18]. At pH 6.0, the cumulative release was slightly higher but still below 50% over 48 h, with a potential peak at 24 h. In contrast, under acidic conditions (pH 4.5), the cumulative release exceeded 50% within 4 h and showed a continuing upward trend. These results demonstrated EGCG-Zn nanoparticles exhibited pH-responsive release behavior. The low release under physiological neutral pH is conducive to prolong circulation *in vivo* and reduce side effects. The rapid release of EGCG in the pH 4.5 medium (mimicking the lysosomal microenvironment) indicates that the nanoparticles are capable of efficient intracellular disassembly, which is favorable for lysosomal escape. RNase degradation assays demonstrated that free siSLC43A2 was degraded within 2 h, whereas siSLC43A2 encapsulated within ACM-EZ/S remained intact even after 6 h (Fig. 2F), confirming the effective protection of ACM-EZ/MS toward siSLC43A2. As shown in Figure S1C, the particle sizes of EZ/MS, AL-EZ/MS, and ACM-EZ/MS remained stable below 100 nm over 7 days. These results demonstrate that ACM-EZ/MS exhibits stability and enables intracellular disassembly, which is of great significance for subsequent *in vitro* and *in vivo* experiments.

Cellular Uptake and Gene Transfection of ACM-EZ/S

To assess the tumor targeting and BBB penetration capacity of ACM-EZ/S, the cellular uptake of the nanoparticles was initially evaluated. After co-incubating different formulations with HCMEC/D3 cells for 4 h, the confocal images in Fig. 3A and Figure S2A demonstrated that both LCM-EZ/S and ACM-EZ/S could significantly adhere to the surface of HCMEC/D_3 cells. This finding is consistent with the previous literatures [19,20], suggesting that glioma cell membranes may possess a certain ability to penetrate the BBB. It has been reported that metastatic cell membranes can achieve tight adhesion interactions through surface receptors on cancer cells and certain endothelial cell adhesion molecules [21]. For GL261 cells, the confocal images in Fig. 3B and Figure S2B clearly showed that the Cy5-labeled siSLC43A2 in the ACM-EZ/S group was successfully delivered into the tumor cells. Furthermore, transwell assay was employed to simulate the BBB *ex vivo* and the penetration capability of the nanoparticles across the BBB was evaluated. As shown in Fig. 3C, HCMEC/D3 cells were pre-seeded on the PET membrane.

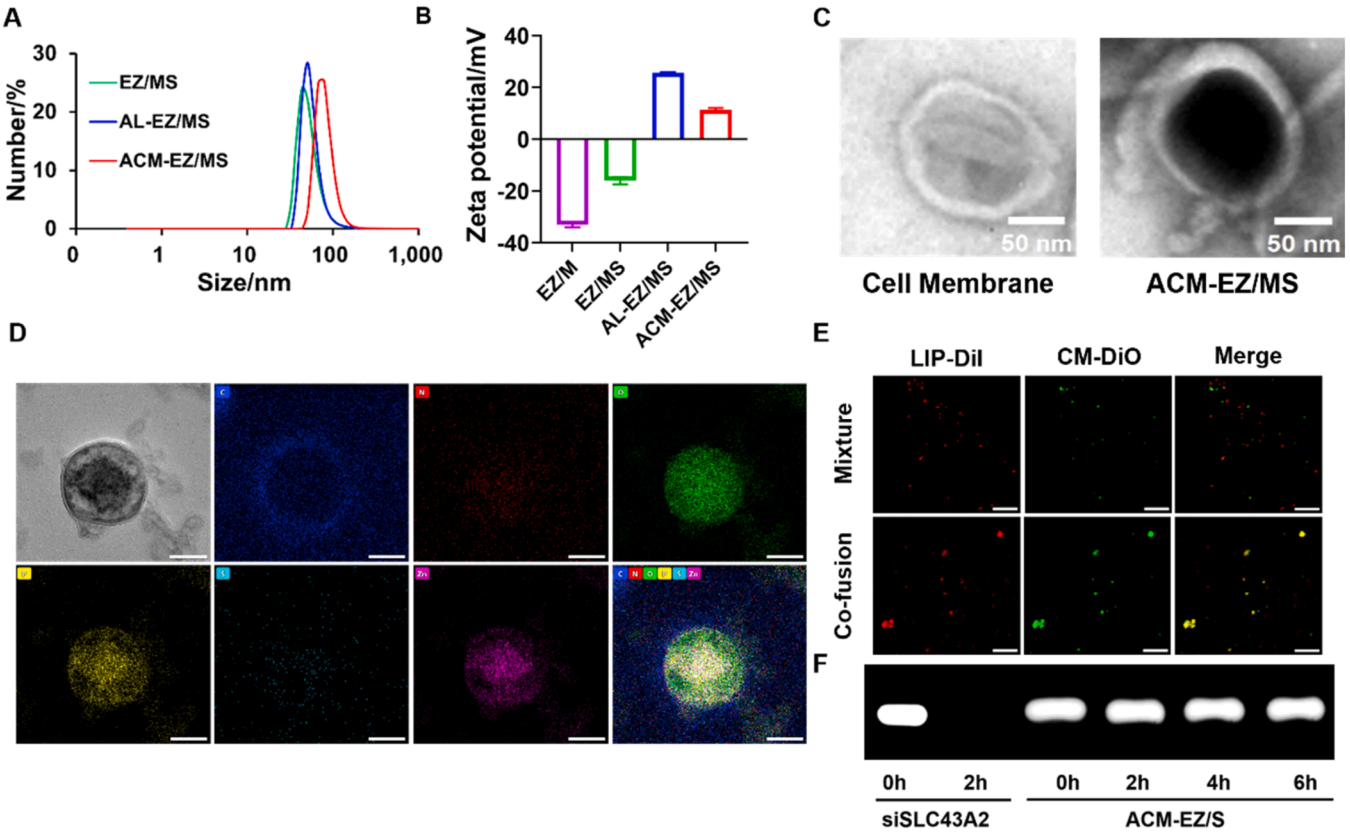

Fig. 2. Characterization of nanoparticles. (A) Hydrodynamic size distribution of EZ/MS, AL-EZ/MS, and ACM-EZ/MS. (B) ζ potential of EZ/MS, AL-EZ/MS, and ACM-EZ/MS. (C) TEM images of cell membrane and ACM-EZ/MS. (D) TEM-EDS image of EZ/MS (scale bar: 50 nm). (E) Confocal Laser Scanning Microscopy (CLSM) images of a physical mixture (LIP/CM) and co-fused sample (ACM) (red: LIP-DiI; green: TNV-DiO; scale bar: 2 μm). (F) Agarose gel electrophoresis demonstrating the gene-protective effect of the carrier on siRNA.

When the trans-endothelial electrical resistance (TEER) reached 100 Ω·cm^2, this indicated the successful establishment of the ex vivo BBB model [22]. GL261 cells were seeded in the lower chamber, while nanoparticles from different groups labeled with cy5-siSLC43A2 were added to the upper chamber. After 24 h, the fluorescence intensity of GL261 cells in the lower chamber was measured by flow cytometry. The results in Fig. 3D showed that the fluorescence intensity of the ACM-EZ/S group was significantly greater than the PBS group ($p < 0.0001$) and the EZ/S group ($p < 0.001$), indicating that the cell membrane-liposome fusion complex (ACM) on the outer layer of EZ significantly enhanced BBB penetration and glioma cell targeting.

The intracellular behavior of the nanoparticles was further investigated. In Fig. 3E, after tumor cells were co-incubated with different nanoparticle formulations for 4 h, confocal laser scanning microscopy (CLSM) images clearly demonstrated that, in contrast to the free Cy5-siSLC43A2 group (where Cy5-siSLC43A2 were totally degraded), the Cy5-siSLC43A2 encapsulated in the ACM-EZ/S nanoparticles exhibited little colocalization with lysosomes, which resulted from the lysosomal rupture and showed efficient lysosomal escape. Following lysosomal escape, siSLC43A2 was released into the cytoplasm. Fig. 3F demonstrated that siSLC43A2 successfully induced a significant down-regulation of the target mRNA transcription level, exerting a more potent inhibitory effect than the positive control (Lipo/siSLC group). Western blot (WB) results (Fig. 3G) further validated the gene silencing effect of siSLC43A2 at the protein level.

In vitro Immunological Mechanisms of ACM-EZ/MS

To investigate the core molecular function of MSA-2, GL261 cells were subjected to serum starvation for 2 h, followed by co-incubation with different formulation groups for 6 h. Then, the cells were further cultured for 48 h with complete culture medium. Western blot (WB) analysis (Fig. 4A) demonstrated that treatment with both ACM-EZ/M and ACM-EZ/MS significantly upregulated the expression of key proteins in the stimulator of interferon genes (STING) pathway in GL261 cells, including phosphorylated TANK-binding kinase 1 (p-TBK1), phosphorylated interferon regulatory factor 3 (p-IRF3), and its downstream effector molecule interferon-beta (IFN-β). Concurrently, the concentration of IFN-β in the cell culture supernatant was measured using an Enzyme-Linked Immunosorbent Assay (ELISA). The results (Figure S3) were consistent with the former WB findings: both the ACM-EZ/M and ACM-EZ/MS groups induced the secretion of high levels of IFN-β. This confirmed the efficient delivery and bioactivity of MSA-2. Furthermore, the secretion level in the ACM-EZ/MS group was significantly higher than that in the ACM-EZ/M group ($p < 0.0001$), suggesting the synergistic effect between MSA-2 and siSLC43A2.

To elucidate the immunomodulatory synergy of ACM-EZ/MS, its underlying immunological mechanisms were further explored. a transwell co-culture model was employed to investigate the impact of siSLC43A2 on the metabolic competition between tumor cells and immune cells (Fig. 4B). CTLL-2 cells were seeded in the upper chamber, while drug-treated GL261 cells were seeded in the lower chamber. Additionally, 30 μM methionine was added to the shared medium. The levels of histone H3K79 di-methylation (H3K79me2) modification in T cells were determined (Figs. 4C and 4D). The results showed that H3K79me2 protein levels were significantly upregulated in the ACM-EZ/S group. As shown in Figs. 4E and 4F, compared to the PBS and ACM-EZ groups, T cells in the ACM-EZ/S group exhibited increased secretion of Interleukin-6 (IL-6) and Tumor Necrosis Factor-α (TNF-α). The increase in H3K79me2 protein levels further promotes T cell

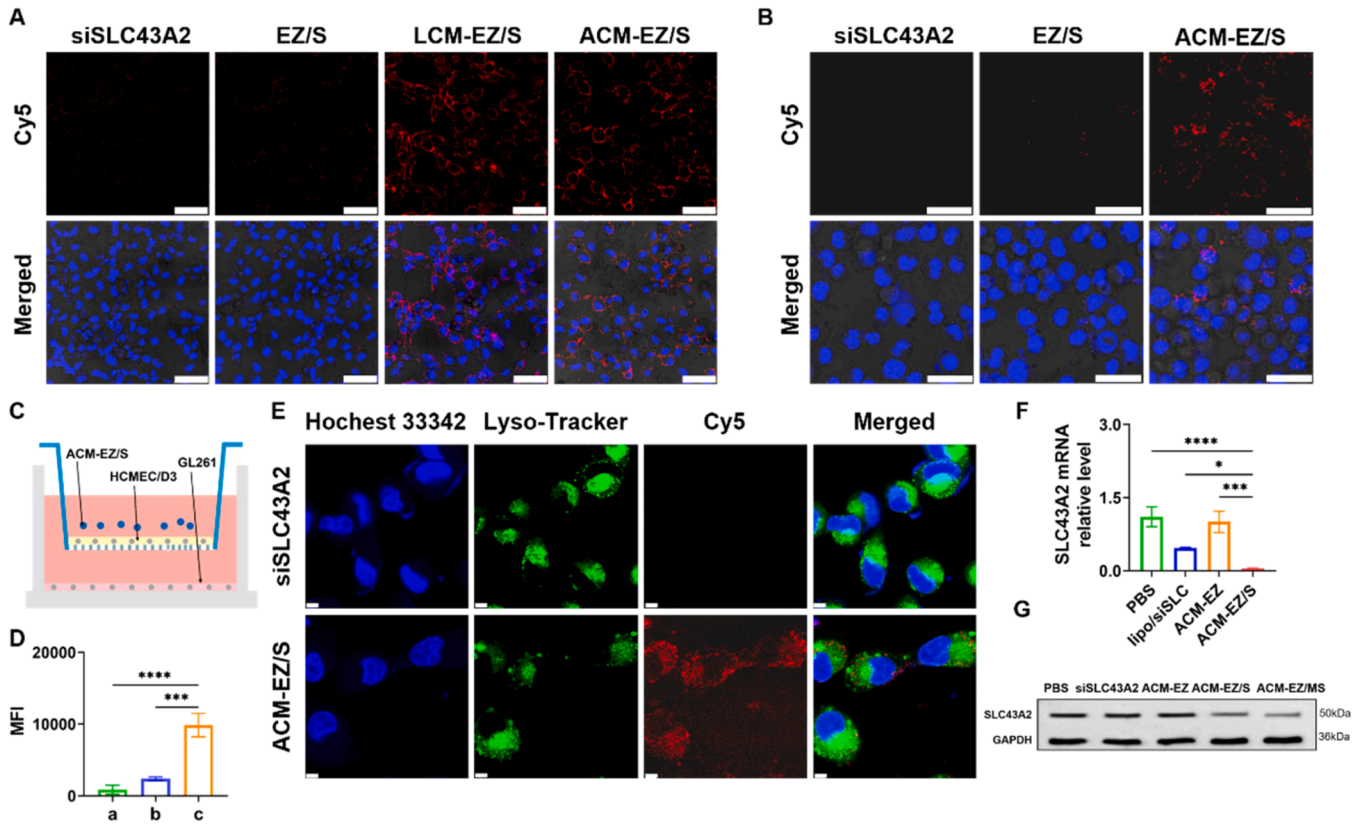

Fig. 3. Evaluation of cellular uptake and gene transfection of ACM-EZ/S. (A) In vitro cellular uptake of siSLC43A2, EZ/S, LCM-EZ/S and ACM-EZ/S in HCMEC/D3 cells visualized by CLSM (blue: nucleus; red: Cy5-siSLC43A2; scale bar: 50 μm).(B) *In vitro* cellular uptake of siSLC43A2, EZ/S and ACM-EZ/S in GL261 cells visualized by CLSM (blue: nucleus; red: Cy5-siSLC43A2; scale bar: 25 μm). (C) Schematic diagram of transwell assay. (D) Fluorescence intensity in the lower-chamber GL261 cells from the quantitative transwell assay (a: siSLC43A2; b: EZ/S; c: ACM-EZ/S; n = 3). (E) *In vitro* lysosome escape of siSLC43A2 and ACM-EZ/S in GL261 cells visualized by CLSM (blue: nucleus; green: lysosomes; red: Cy5-siSLC43A2; scale bar: 5 μm). (F) *In vitro* SLC43A2 mRNA expression levels in GL261 cells treated with various formulations determined by RT-qPCR. (n = 3) (G) *In vitro* SLC43A2 protein expression levels in GL261 cells treated with various formulations determined by WB.

survival and inhibits T cell apoptosis [12] (Fig. 4 G, S4A). The enhanced secretion of inflammatory factors from T cells subsequently promotes tumor cell apoptosis (Figure 4H, S4B).

The mechanistic studies untangle a clear synergistic pathway: On one hand, ACM-EZ/MS activates the STING pathway in tumor cells via MSA-2, thereby initiating a systemic immune response; on the other hand, it achieves precise metabolic intervention through siSLC43A2. This intervention intrinsically orchestrates epigenetic reprogramming and functional activation in T cells at the intracellular level. These two pathways synergistically orchestrate the establishment of anti-tumor immune microenvironment, which not only potently activates anti-tumor immune responses but also facilitates T cell survival, persistence, and effector function.

Antitumor Effects and Mechanisms of the ACM-EZ/MS in Ectopic Glioma Models

Following the verification of the *in vitro* mechanism of MSA-2 and siSLC43A2 in ACM-EZ/MS (Figs. 3 and 4), we further evaluated their *in vivo* therapeutic potential. Given that MSA-2 functions as the immune agonist, the ACM-EZ/M group (MSA-2-loaded) and ACM-EZ/MS group (MSA-2 and siSLC43A2 co-loaded) were prioritized in the *in vivo* experiments, with the purpose of clarifying the efficacy of MSA-2 monotherapy and the immune-potentiating effect of siSLC43A2. Additionally, to assess their clinical therapeutic performance, temozolomide (TMZ), a clinically standardized chemotherapeutic agent, was incorporated as a positive control. The administration scheme for mice is shown in Fig. 5A. Before administration, a preliminary exploration into the *in vivo* distribution of the ACM-EZ/MS was conducted in the ectopic glioma model. Cy5-siSLC43A2 was employed to track its distribution within different formulations. The major organs (i.e., heart, liver, spleen, lungs, kidneys) and tumors were harvested from C57BL/6 mice in all treatment groups at 24 h post-administration. The *ex vivo* images (Fig. 5B) showed that the EZ/S, LCM-EZ/S, and ACM-EZ/S groups all exhibited a certain level of siSLC43A2 accumulation in the liver, lungs, and kidneys. This observation is consistent with the typical biodistribution pattern of intravenously administered nanoparticles being sequestered by the mononuclear phagocyte system (MPS) [23–25]. Notably, the ACM-EZ/S group displayed the strongest signal in the liver, suggesting that its unique surface modification (Ang-2 peptide and cell membrane) may alter its interaction with the reticuloendothelial system (RES). Concomitantly, the ACM-EZ/S group exhibited intense and specific fluorescence signal at the tumor site, indicating that the Ang-2 peptide-mediated active targeting capability, in conjunction with the homologous targeting of the cell membrane coating. These designs enable the efficient tumor accumulation, which laid a solid foundation for targeted glioma therapy. Subsequently, treatment was administered in accordance with the administration scheme depicted in Fig. 5A. As shown in Figs. 5C and 5D, tumor volume in the ACM-EZ/MS group was numerically lower than in the TMZ group, suggesting a mild trend of improved antitumor efficacy with this biomimetic nanocarrier. Nevertheless, ectopic glioma lacks the BBB and exhibits distinct immunosuppressive and metabolic profiles compared with orthotopic glioma. Consequently, the BBB penetration, targeted accumulation, and synergistic immunotherapeutic effects mediated by ACM-EZ/MS were not fully manifested, resulting in no statistically significant difference in

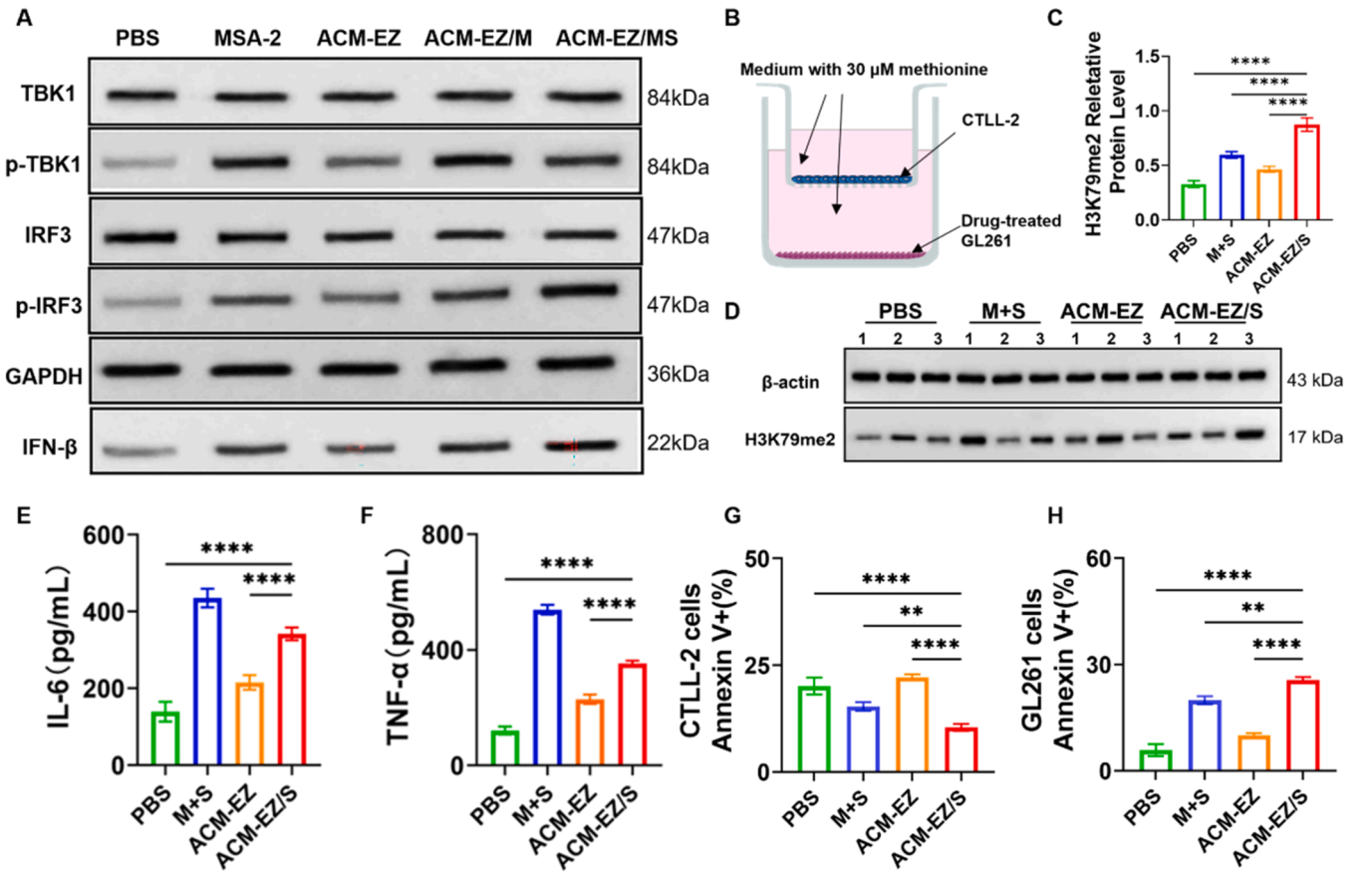

Fig. 4. *In vitro* immunological mechanisms of ACM-EZ/MS. (A) *In vitro* TBK1, p-TBK1, IRF3, p-IRF3, IFN-β protein expression levels in GL261 cells treated with various formulations determined by WB. (B) Schematic diagram of the co-culture of CTLL-2 cells and drug-treated GL261 cells in a 30 μM methionine environment. (C) Relative Quantitative Expression Analysis of H3K79me2 Protein. (D) *In vitro* H3K79me2 protein expression levels within CTLL-2 cells as determined by WB (n = 3). (E) IL-6 secretion and (F) TNF-α secretion levels from CTLL-2 cells co-cultured with GL261 cells treated with different formulation groups, n = 3. (G) Apoptosis of CTLL-2 cells and (H) GL261 cell in the co-culture system was assessed by flow cytometry, n = 3.

therapeutic efficacy between the two groups. In addition, after 15 days of treatment, both ACM-EZ/M and ACM-EZ/MS significantly inhibited tumor growth compared with the glucose solvent control group (Glu group) ($p < 0.0001$). These results are further supported by *ex vivo* tumor images in Fig. 5E, which clearly show smaller tumor volumes in the ACM-EZ/M and ACM-EZ/MS groups than in other groups.

Following treatment with different formulations, tumor tissues were collected to investigate the molecular mechanisms underlying the antitumor effects. Firstly, the target gene (siSLC43A2) silencing efficacy of the formulations was validated. Fig. 5F demonstrated that, compared with the control group, ACM-EZ/MS significantly downregulated the mRNA transcription level of the target gene. Fig. 5 G and S5A further confirmed that ACM-EZ/MS also exerted a silencing effect at the protein level. The reduced SLC43A2 expression under TMZ treatment reflects a compensatory metabolic adaptation in glioma cells. TMZ-induced DNA damage activates AMPK and inhibits mTORC1 [26,27], which block protein synthesis and promotes amino acid recycling through autophagy and proteasomal degradation [28,29]. To preserve intracellular amino acids and maintain amino acid homeostasis under suppressed anabolism, glioma cells downregulate the amino acid efflux transporter SLC43A2 [30], thereby reducing amino acid loss and sustaining metabolic homeostasis during chemotherapy stress. Subsequently, we explored the preliminary immune mechanism underlying the antitumor effect of MSA-2. The protein levels of p-TBK1 and p-IRF3 in the ACM-EZ/M and ACM-EZ/MS groups were markedly upregulated relative to the control group (Figures 5H, S5B, and S5C). Additionally, the IFN-β secretion level in the ACM-EZ/M and ACM-EZ/MS groups was also significantly elevated (Fig. 5I), with the ACM-EZ/MS group exhibiting a significantly higher level than the ACM-EZ/M group ($p < 0.001$), providing evidence for the synergistic effect between MSA-2 and siSLC43A2. Especially, despite the marked secretion level of inflammatory cytokines exhibited by the M+S group in cellular assays, its antitumor efficacy failed to meet expectations in *in vivo* experiments. The core underlying reason is that free MSA-2 and free siRNA are prone to rapid clearance in the *in vivo* milieu, thus being unable to efficiently accumulate at the target site to exert their therapeutic effects.

The aforementioned results demonstrate that ACM-EZ/MS can successfully activate the STING signaling pathway and downregulate SLC43A2 expression in tumor cells. To elucidate how these core molecular events translate into a coordinated anti-tumor immune response, we examined the therapy-induced activating of the tumor immune microenvironment. Tumor tissues from different treatment groups were harvested, enzymatically dissociated into single-cell suspensions, which were subsequently subjected to flow cytometric analysis. As shown in Fig. 5J, Figure S6A, Fig. 5K and Fig. 5M, compared with the Glu, M+S, and ACM-EZ groups, the proportions of intratumoral mature dendritic cells and tumor-infiltrating $CD8^+$ T cells were significantly elevated in both the ACM-EZ/M and ACM-EZ/MS groups ($p < 0.001$). These findings suggest that, following efficient delivery into tumor cells, MSA-2 can alleviate the immunosuppressive constraints within the local tumor immune microenvironment. The increases across multiple immune-cell subsets were significantly more pronounced in the ACM-EZ/MS group than in the ACM-EZ/M group ($p < 0.0001$), consistent with a synergistic immunomodulatory interaction between siSLC43A2 and MSA-2. Besides, the proportion of apoptotic $CD8^+$ T cells within tumors was reduced in both the ACM-EZ/M and ACM-EZ/MS groups

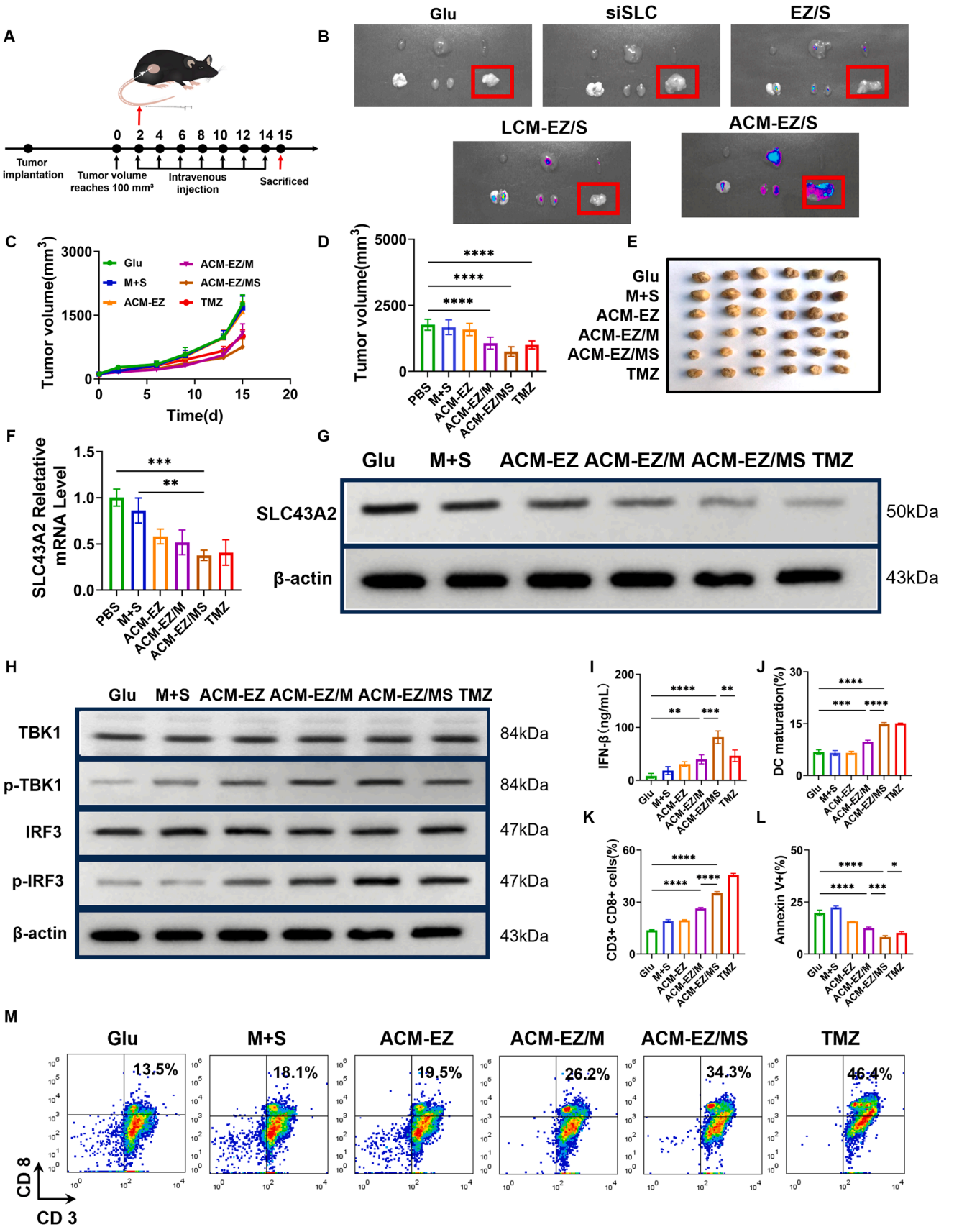

(caption on next page)

Fig. 5. Antitumor Effects and Mechanisms of ACM-EZ/MS in Ectopic Glioma Models. (A) Schematic diagram of the administration schedule in the ectopic glioma model. (B) Biodistribution of different formulations in various organs at 24 h post-intravenous administration in C57BL/6 mice (top row, from left to right: heart, liver, spleen; bottom row, from left to right: lung, kidney, tumor). (C) Changes in tumor volume over 15 days, n = 6. (D) Tumor volume of different formulation groups on day 15 (n = 6). (E) Representative photographs of excised tumors from C57BL/6 mice after 15 days of treatment with different formulations. (F) In vivo SLC43A2 mRNA expression levels in tumor tissues treated with various formulations as determined by RT-qPCR, n = 3. (G) In vivo SLC43A2 protein expression levels in tumor tissues treated with various formulations as determined by WB, n = 3. (H) In vivo protein expression levels of TBK1, p-TBK1, IRF3, and p-IRF3 in tumor tissues treated with various formulations as determined by WB, n = 3. (I) In vivo IFN-β protein expression levels in tumor tissues treated with various formulations as determined by ELISA, n = 3. (J) In vivo mature dendritic cells (DCs) in tumor tissues treated with various formulations determined by flow cytometry, n = 3. (K) In vivo $CD8^+$ T cells in tumor tissues treated with various formulations determined by flow cytometry, n = 3. (L) In vivo apoptosis of $CD8^+$ T cells in tumor tissues treated with various formulations determined by flow cytometry, n = 3. (M) In vivo $CD8^+$ T cells in tumor tissues treated with various formulations determined by flow cytometry. To align with the clinical translation and maximize the *in vivo* therapeutic efficacy, the animal study employed the MSA-2 mono-delivery formulation group (ACM-EZ/M) and the MSA-2 & siSLC43A2 co-delivery group (ACM-EZ/MS). The single siSLC43A2-loaded formulation (ACM-EZ/S) was not included in the *in vivo* experimental groups and was only used for *in vitro* mechanistic characterization.

(Fig. 5L and Figure S6B), indicating that MSA-2 could efficiently improve $CD8^+$ T cell viability in the tumor microenvironment. Concurrently, the proportion of apoptotic $CD8^+$ T cells in the ACM-EZ/MS group was statistically lower than that in the ACM-EZ/M group ($p < 0.001$). This result supports a synergistic contribution of the co-delivered siSLC43A2: building on the MSA-2–mediated recruitment and activation of $CD8^+$ T cells, SLC43A2 silencing may further enhance a survival-permissive niche by metabolically reprogramming tumor cells and thereby alleviating local metabolic constraints on T-cell fitness. Immunofluorescence staining results (Figure S6C) visually confirmed that the ACM-EZ/MS group exhibited the highest level of $CD8^+$ T cell infiltration.

We also monitored immune-related cytokines in the ectopic glioma model. The concentration of IL-6 and TNF-α in both tumor tissues and serum were reduced in the ACM-EZ/M and ACM-EZ/MS groups (Figure S7, S8C, S8D). The reduced levels of these two cytokines are attributed to the suppressed function of their main secretory cells—M2-type tumor-associated macrophages (TAMs) and myeloid-derived suppressor cells (MDSCs) [31–33], suggesting attenuation of the pro-tumor inflammatory microenvironment and a shift toward a specific anti-tumor immune response. Simultaneously, serum IFN-β levels were elevated in mice from the ACM-EZ/M and ACM-EZ/MS groups (Figure S8A), corroborating the observed upregulation trend of IFN-β expression in tumor tissues (Fig. 5I). The increased serum methionine levels in mice from the ACM-EZ/MS group (Figure S8B) were also consistent with the trends presented in Fig. 5 F, 5 G, and S5A. Collectively, these findings demonstrate that ACM-EZ/MS achieves therapeutic efficacy in the ectopic glioma and is supported by a well-defined immunological mechanism, which provides a strong rationale for subsequent evaluation in an orthotopic glioma model.

Antitumor Effects and Mechanisms of the ACM-EZ/MS in Orthotopic Glioma Models

To ultimately validate the therapeutic efficacy of ACM-EZ/MS against clinically relevant intracerebral lesions, we explored its performance in an orthotopic glioma model, with emphasis on BBB penetration, tumor targeting, and antitumor efficacy. Fig. 6A illustrates the administration scheme in C57BL/6 mice. Firstly, the tumor-targeting ability was assessed via *in vivo* imaging system, with Cy5-siSLC43A2 served as the fluorescent traces. Following administration, imaging was performed at 0 h, 4 h, 12 h, and 24 h post-treatment. Fig. 6B reveals that the EZ/S, LCM-EZ/S, and ACM-EZ/S groups were all capable of crossing the BBB and accumulating at the intracerebral tumor locus. Among these, ACM-EZ/S showed significantly higher targeting specificity for brain tumors relative to controls ($p < 0.0001$). This observation confirms that the Ang-2 peptide and cell membrane modification synergistically endow the nanoparticles with superior active tumor-targeting. Stably luciferase-expressing G261 cells were utilized for the construction of the orthotopic glioma model. Fig. 6C shows that no significant difference in tumor bioluminescence signal intensity was detected among all groups initially. After two-week treatment, compared with the Glu group, the M+S group showed only limited tumor suppression, while both the ACM-EZ/M and ACM-EZ/MS groups achieved marked suppression of tumor growth ($p < 0.05$). Among them, the ACM-EZ/MS group showed the most prominent antitumor effect, even outperforming TMZ, the first-line clinical chemotherapeutic drug. These results verify that the biomimetic co-delivery system can exert excellent *in vivo* antitumor activity through efficient tumor targeting.

Following the treatment, tumor tissues were collected to investigate the molecular mechanisms underlying the antitumor effects. Immunofluorescence staining results (Figure 6D, S9) visually indicated the ACM-EZ/MS group exhibited the lowest level of siSLC43A2 protein expression. WB results (Figure 6E, S10) also confirmed that the SLC43A2 protein expression in the ACM-EZ/MS group was markedly reduced relative to other experimental groups. These results indicate that ACM-EZ/MS successfully delivers siSLC43A2 to the intracranial tumor loci and achieves targeted gene silencing. To elucidate the downstream immune regulatory mechanisms, we further analyzed the activation status of the STING signaling pathway in tumor tissues. WB results (Figs. 6F, 6G, and 6H) revealed that, the expression levels of key signaling molecules p-TBK1 and p-IRF3 were significantly upregulated in the tumor tissues of the ACM-EZ/M and ACM-EZ/MS groups ($p < 0.01$). Concurrently, IFN-β levels in the tumor tissues were also significantly elevated ($p < 0.01$, Figure S11). The ACM-EZ/MS group exhibited higher levels of p-IRF3 and IFN-β than the ACM-EZ/M group, suggesting the synergistic effect mediated by the combination of siSLC43A2 and MSA-2.

Mechanisms of Activating the Immune Microenvironment by ACM-EZ/MS in Orthotopic Glioma

Subsequently, we dissected the mechanism by which ACM-EZ/MS activates the immune microenvironment of orthotopic glioma. First, we assessed the infiltration and activation of key immune cell subsets. As illustrated in Figs. 7A and 7B, the ACM-EZ/M and ACM-EZ/MS groups exhibited higher infiltration and activation levels of DCs and $CD8^+$ T cells compared with the Glu group and other control groups ($p < 0.0001$), indicating that MSA-2 was successfully delivered to the glioma site and exerted potent immunostimulatory effect. The number of immune cell populations in the ACM-EZ/MS group was significantly greater than that in the ACM-EZ/M group ($p < 0.0001$), suggesting an immunomodulatory synergistic effect between siSLC43A2 and MSA-2. In Fig. 7C, the proportion of apoptotic $CD8^+$ T cells in tumor tissues was reduced in the ACM-EZ/M and ACM-EZ/MS groups ($p < 0.0001$), with ACM-EZ/MS group exhibiting an even lower rate relative to the ACM-EZ/M group. This indicates that MSA-2 can ameliorate the tumor immune microenvironment and inhibit $CD8^+$ T cell apoptosis, while SiSLC43A2 further optimizes the metabolic environment for $CD8^+$ T cells. The immunofluorescence results (Fig. 7D) corroborated the flow cytometry data presented in Fig. 7B. We also evaluated the immune environment of cerebrospinal fluid (CSF). As depicted in Figs. 7E and 7F, the elevated level of IFN-β and methionine confirm the successful delivery of MSA-2 and siSLC43A2 to the intracranial tumor loci, respectively. The reduced levels of IL-6 and TNF-α in both CSF and tumor

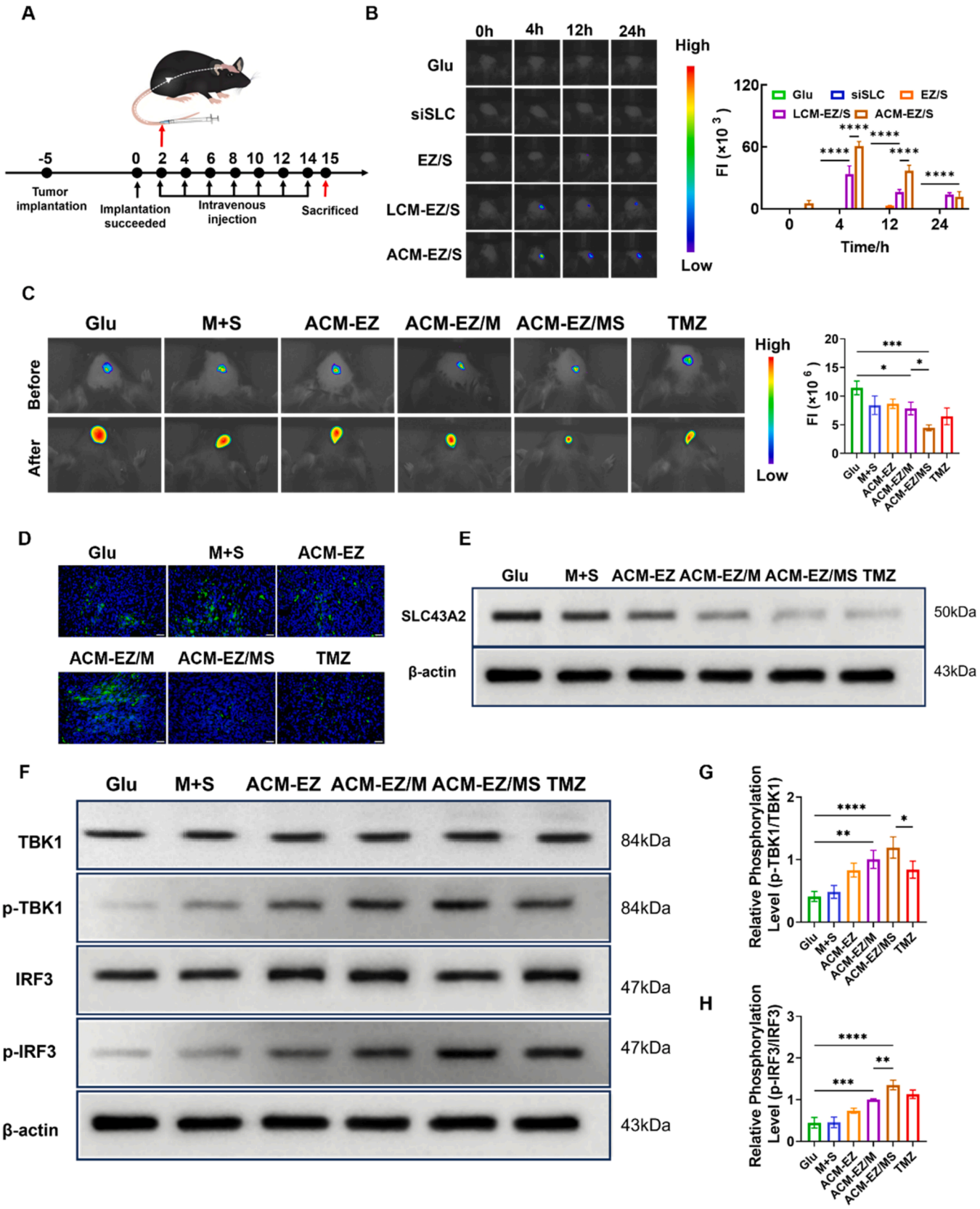

Fig. 6. Antitumor Effects and Mechanisms of ACM-EZ/MS in Orthotopic Glioma Models. (A) Schematic diagram of the administration regimen in the orthotopic glioma model. (B) Intracerebral Tumor targeting of different formulations in C57BL/6 mice within 24 h after intravenous injection via the tail vein. (C) Antitumor effects of different formulations in C57BL/6 mice, n = 3. (D) Immunofluorescence staining results for the SLC43A2 protein in brain tumors from mice treated with different formulations (blue: nucleus; green: SLC43A2 protein; scale bar: 50 μm). (E) *In vivo* SLC43A2 protein expression levels in tumor tissues treated with various formulations determined by WB, n = 3. (F) *In vivo* TBK1, p-TBK1, IRF3, and p-IRF3 protein expression levels in tumor tissues treated with various formulations determined by WB, n = 3. (G) Relative quantitative expression analysis of p-TBK1/TBK1 protein and (H) p-IRF3/IRF3 protein.

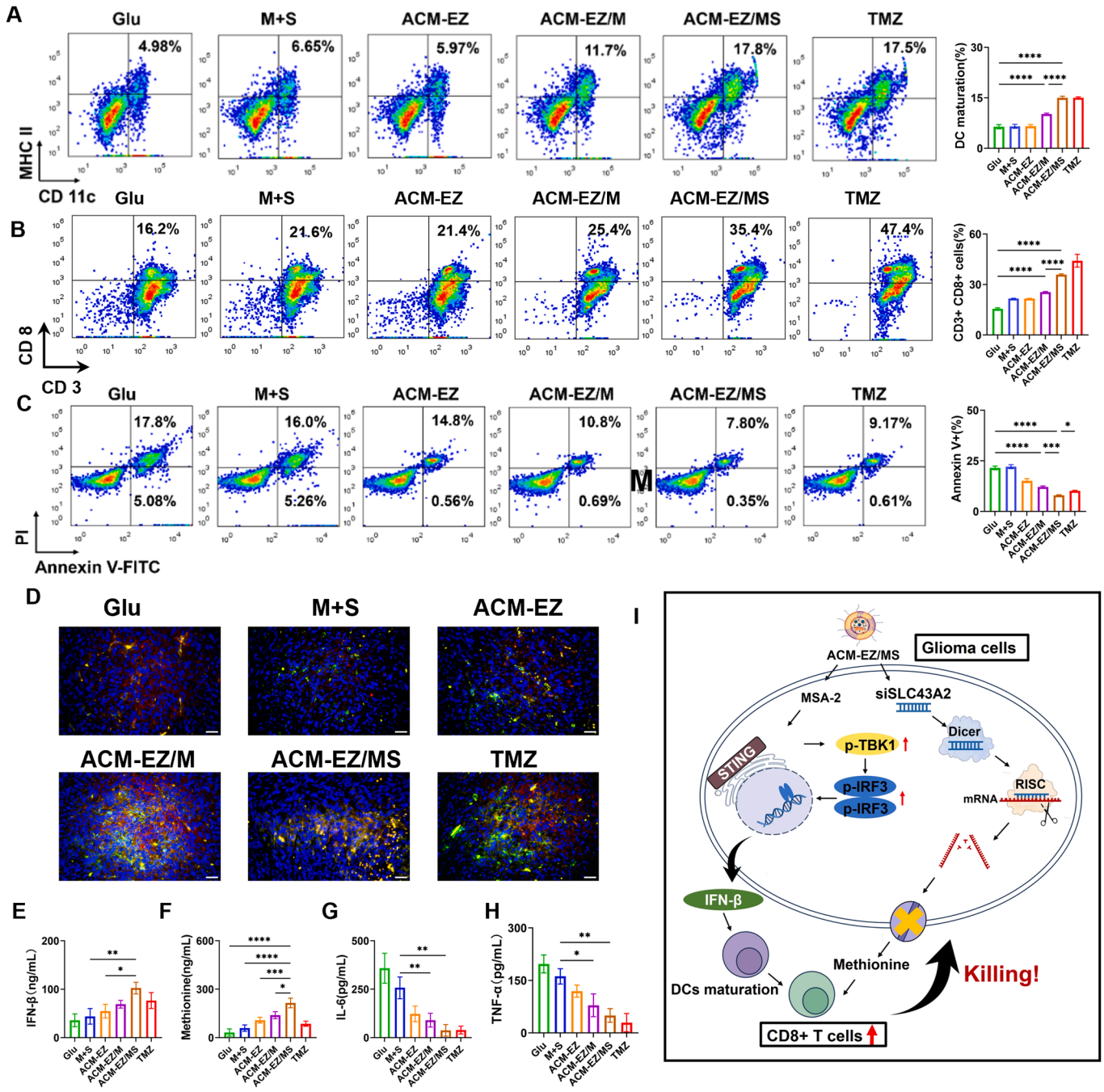

Fig. 7. Mechanisms of Activating the Immune Microenvironment by ACM-EZ/MS in Orthotopic Glioma. (A) *In vivo* mature DCs in tumor tissues treated with various formulations determined by flow cytometry, n = 3. (B) *In vivo* $CD8^+$ T cells in tumor tissues treated with various formulations determined by flow cytometry, n = 3. (C) *In vivo* apoptosis of $CD8^+$ T cells in tumor tissues treated with various formulations determined by flow cytometry, n = 3. (D) Immunofluorescence staining of anti-CD3 and anti-CD8 in tumor tissues (green: anti-CD3; red: anti-CD8; scale bar: 50 μm). (E) *In vivo* IFN-β expression levels in the cerebrospinal fluid (CSF) of mice treated with various formulations determined by ELISA, n = 3. (F) *In vivo* methionine levels in the CSF of mice treated with various formulations determined by ELISA, n = 3. (G) *In vivo* IL-6 levels and (H) TNF-α levels in the CSF of mice treated with various formulations determined by ELISA, n = 3. (I) Schematic diagram of the mechanism by which ACM-EZ/MS exerts immunopotentiating effects to kill tumor cells.

tissues (Fig. 7 G, 7H, and S12) further validate the establishment of a favorable anti-tumor immune microenvironment.

In summary, the mechanism by which ACM-EZ/MS activates the antitumor immune microenvironment is consistent across both ectopic and orthotopic glioma models, as schematically illustrated in Fig. 7I. The biomimetic co-delivery system ACM-EZ/MS can effectively activate the STING pathway to induce DC maturation and $CD8^+$ T cells infiltration, while concurrently suppressing the SLC43A2 expression to enhance $CD8^+$ T cell survival. This combination strategy collectively mediates efficient tumor cells killing, exerting superior anti-tumor efficacy.

Safety Evaluation of ACM-EZ/MS

Finally, a preliminary biosafety assessment of ACM-EZ/MS was conducted. The *in vitro* cytotoxicity of the formulation against tumor cells at various concentrations was assessed using the MTT assay. As shown in Figure S13A, at the formulation concentration of 0.1 mg/mL used in our study, no significant cytotoxicity against tumor cells was

observed. Subsequently, the *in vivo* safety profile of the formulation was further investigated. As shown in Figures S13B and S13C, no significant changes in body weight of mice bearing ectopic or orthotopic glioma models were observed in the ACM-EZ/M and ACM-EZ/MS groups compared to the Glu group over the 15-day administration period, suggesting good overall tolerability. To evaluate the potential systemic toxicity of ACM-EZ/MS, serum biochemical parameters were measured on days 0, 7, and 14. In Figure S13D, lactate dehydrogenase (LDH) levels showed a slight initial decrease followed by a minor increase, suggesting a possible transient effect on cell membrane stability or mild tissue stress during the early phase of treatment [34,35]Alkaline phosphatase (ALP), alanine aminotransferase (ALT), and aspartate aminotransferase (AST) levels, which are associated with liver function, are presented in Figures S13E, S13F, and S13G, respectively. The decrease in ALP and ALT may be attributed to a mild inhibition of certain hepatic metabolic activities or enzyme synthesis by the formulation, which is not indicative of liver injury (as injury would typically elevate these markers [36]). The trend observed for AST was also consistent with that of LDH, reinforcing the reliability of the findings and indicating a minor, transient alteration in hepatocyte stability during the initial treatment phase, followed by stabilization. A slight change in uric acid (UA) levels (Figure S13H) suggested a minor, physiological adjustment in renal excretion function. A slight decrease in blood urea nitrogen (UREA) levels (Figure S13I) indicated a minor reduction in protein metabolism, which is considered within the normal range. The slight decrease in triglycerides (TG) (Figure S13J) was likely related to animal energy expenditure and represents a benign change [37]. Overall, ACM-EZ/MS did not exhibit acute or pronounced toxic effects, with all observed variations being mild. Hematoxylin and eosin (H&E) staining results (Figure S14) revealed no significant pathological abnormalities in heart, liver, spleen, lungs, or kidneys among the treatment groups, indicating that ACM-EZ/MS did not cause detectable histopathological damage.

Discussion

This study successfully constructed a multifunctional biomimetic nano-delivery system designed to potentiate anti-glioma immune response through the synergistic activation of STING pathway and amelioration of metabolic suppression. Our results demonstrated that this system effectively inhibited tumor growth in orthotopic gliomas. The therapeutic outcomes primarily relied on the stepwise resolution of the following key issues:

1. Structural advantages of nanocarriers

   First, the outer cell membrane and Ang-2 peptide-modified liposomes can facilitate the penetration of nanoparticles across the BBB. Membrane-retained surface proteins (e.g., adhesion-or recognition-related components) may mediate a basal affinity for BBB endothelial cells [38]. Beyond this passive membrane-mediated effect, the Ang-2 peptide provides an active transcytosis mechanism. The Ang-2 peptide specifically binds to the extracellular ligand-binding domain of LRP1 on brain microvascular endothelial cells, followed by internalization via clathrin-dependent endocytosis. After undergoing intracellular sorting and trafficking in early endosomes, the complex finally accomplishes transcytosis across endothelial cells, thereby mediating the release of the carrier into the brain parenchyma [39–41]. Furthermore, the LRP1-mediated transport pathway can bypass P-glycoprotein-mediated efflux, thereby further boosting the specific accumulation of therapeutics in the brains [42]. After crossing the BBB, the homologous cell membrane further endowed the carrier with a homing capability. The protein ligands on the membrane surface could bind to specific receptors on the tumor cell surface, mediating active targeting and achieving efficient enrichment of the drug within intracranial glioma lesions [43,44]. Finally, following uptake by tumor cells, the acidic lysosomal environment triggers drug release: the outer lipid layer mediates membrane disruption [45,46], the internal EGCG-Zn^{2+} complex dissociates under low pH, and the proton sponge effect promotes lysosomal rupture, allowing siSLC43A2 and MSA-2 to enter the cytoplasm and exert their functions [47,48].
2. Synergistic effects of effector molecules

   Encapsulation within the outer carrier addresses the major formulation barriers for the two agents—enhancing the circulation stability and tumor-targeted delivery for hydrophobic MSA-2 and hydrophilic siSLC43A2. Upon release into the cytoplasm, MSA-2 directly activates the STING pathway, driving downstream TBK1/IRF3 phosphorylation and IFN-β responses, thereby initiating innate immune activation and1 promoting immune cell recruitment. Concurrently, siSLC43A2 downregulates SLC43A2 expression, reducing methionine uptake in tumor cells. On one hand, the decreased intracellular methionine content leads to lower SAM levels, which inhibits the carboxymethylation and maturation of nuclear lamins [16], resulting in DNA methylation dysregulation and the release of chromatin fragments into the cytoplasm [17]. On the other hand, it indirectly enhances methionine uptake by T cells, improving nutrient availability and promoting $CD8^+$ T cell survival, thereby cooperating with MSA-2 to potentiate immune responses. Collectively, the two agents achieve a precise spatiotemporally synergy by simultaneously activating immunity and relieving immunosuppression.
3. Favorable synergistic therapeutic efficacy of the system *in vitro* and in *vivo*

In vitro experimental results demonstrated that the co-delivery of siSLC43A2 and MSA-2 could markedly enhance the immune response in tumor cells. In both subcutaneous and orthotopic glioma models, this nanosystem can effectively cross the BBB and accumulate at the tumor site. It synergistically regulates tumor metabolism and the immune microenvironment, inhibits tumor growth, and achieves superior and highly efficient synergistic therapeutic effects compared with temozolomide.

In summary, this study not only demonstrates the feasibility of a synergistic immunotherapy but also, through the layer-by-layer progressive design of the carrier, systematically addresses multiple key challenges in delivering nanomedicines into glioma cells. In addition, compared with current immunotherapeutic agents for glioma, the delivery platform constructed in this study displays clear advantages in delivery efficiency and antitumor efficacy. Specifically, the Ang 2-functionalized biomimetic shell facilitates enhanced BBB traversal and targeted tumor accumulation. The metal-phenolic core supports excellent co-delivery stability and high drug loading. The dual regulation of the tumor immune and metabolic microenvironments collectively contributes to superior synergistic therapeutic effects.

The nanodelivery system developed in this study still presents numerous scientific issues that need to be urgently addressed. At the present stage, systematic investigations into its biosafety and *in vivo* fate have not been performed, and these aspects require comprehensive and in-depth elucidation using more refined animal models and omics approaches [2,49,50]. Nevertheless, we expect that this design strategy will expedite the development of efficient nanomedicines for the treatment of central nervous system disorders.

Materials and methods

Materials

EGCG was obtained from shsendpharm Co., Ltd. (Shanghai, China). Dopamine hydrochloride and Zinc acetate dihydrate were sourced from Macklin Biochemical Co., Ltd (Shanghai, China). MSA-2 was purchased from InvivoChem (USA). SiSLC43A2 and related PCR primers were synthesized by GenePharma Co.,Ltd (Shanghai, China). Green qPCR MasterMix was procured from BioMed (Beijing, China). 1,2-Distearoyl-

sn-glycero-3-phosphocholine (DSPC) and (2,3-Dioleyl-propyl) -trimethylamine (DOTAP) were supplied by Macklin Biochemical Co., Ltd (Shanghai, China). Cholesterol was purchased from RHAWN (Shanghai, China). 1,2-Distearoyl-sn-glycero-3-phosphoethanolamine-polyethylene glycol-3400-Angiopep-2 (DSPE-PEG$_{3400}$-Ang-2) was custom-synthesized by Tanshtech Co., Ltd (Guangzhou, China). Fluorescence -conjugated antibodies, including PE-Cy7-anti-I-A/I-E, BV510-anti-CD45, were obtained from BioLegend. Inc (USA). PerCP-cy5.5-anti-CD3e, APC-cy7-anti-CD8a, FITC-anti-CD4 were purchased from BD Biosciences (USA). Primary Antibodies against TBK1, IRF3, p-TBK1, p-IRF3, IFN-β were purchased from Cell Signaling Technology. Inc (USA). Anti- SLC43A2 was obtained from Proteintech Group, Inc (Wuhan, China). Anti-IRF3 was purchased from Beyotime Biotechnology (Shanghai, China). The fluorescent dyes DiO and DiI were purchased from KeyGEN BioTECH Corp., Ltd (Jiang Su, China).

Cell Lines

The murine glioma cell lines GL261 and GL261-Luc, as well as the human brain microvascular endothelial cell line HCMEC/D_3, were obtained from iCell Bioscience Inc (Shanghai, China). Cells were cultured in DMEM supplemented with 10% fetal bovine serum (FBS) and 1% penicillin-streptomycin (PS), and cultured at 37 °C with 5% CO_2. The CTLL-2 cell line and its corresponding culture medium were purchased from Procell (Wuhan, China). The cells were maintained under standard conditions (37 °C, 5% CO_2) according to the supplier's recommendations.

Animal experiments

All SPF animals were kept in the Animal Facility Center of Capital Medical University. All animal procedures were conducted in accordance with institutional guidelines and were reviewed and approved by the Institutional Animal Care and Use Committee (IACUC) of Capital Medical University (Approval No.: AEEI-2025–849).

Preparation of ACM-EZ/MS

The preparation of the EZ/MS core was optimized based on the procedure reported by Li et al. [1]. Briefly, the reaction was conducted in 15 mL of 0.1 M phosphate buffer (PB, pH 7.4) under vigorous stirring (1100 rpm). A methanolic pre-mix containing EGCG (4.50×10^{-6} mol), dopamine (5.00×10^{-7} mol), and MSA-2 (6.795×10^{-7} mol) was added, followed by the addition of Zn^{2+} solution (4.00×10^{-5} mol) to initiate assembly.

The reaction was allowed to proceed at room temperature in the dark for 20 min. The resulting product was collected in a 30 kDa molecular weight cut-off (MWCO) ultrafiltration tube (5000 rpm, 15 min) to remove unbound components, followed by an additional rinse with 200 μL of 0.1 M PB (pH 8.0) (5000 rpm, 5 min) to further eliminate residual free MSA-2. Finally, the nanoparticles were washed with 200 μL deionized water (5000 rpm, 5 min). EZ/MS was obtained by incubating purified EZ/M nanoparticles with siSLC43A2 (6 μg) at room temperature for 4 h.

GL261 cell membranes were isolated using a gradient centrifugation method. Cells in the culture dish were harvested and treated with an ultrasonic cell disruptor for 2 min. The supernatant was collected by low-speed centrifugation (700 rpm, 10 min), followed by high-speed centrifugation of the supernatant (13,000 rpm, 30 min) to obtain the cell membrane pellet.

Liposomes encapsulating the EZ/MS nanoparticles were prepared via the reverse-phase evaporation method. In brief, DSPC, cholesterol, DSPE-PEG$_{3400}$-Ang-2 and DOTAP (molar ratio 29: 17: 1: 8) were dissolved in chloroform to form the organic phase, which was combined with an aqueous phase of EZ/MS nanoparticles at an organic-to-aqueous volume ratio of 3:1. A stable water-in-oil (W/O) primary emulsion was formed by probe sonication. Subsequently, the organic phase was removed by rotary evaporator at 35℃ to yield a liposomal suspension containing the encapsulated nanoparticles.

To construct the biomimetic delivery system, isolated GL261 membranes were mixed with the nanoparticle-loaded liposomes at a 1:1 (w/w) ratio. Membrane–liposome fusion was induced by sonication in an ice bath for 15 min. Unfused components were removed by low-speed centrifugation (1000 rpm, 5 min), yielding the cell membrane-camouflaged biomimetic nanoparticles.

Characterization of Nano delivery Systems

The particle size and zeta potential of the nanoparticles were characterized by dynamic light scattering (DLS). The morphology was characterized by transmission electron microscopy (TEM), and elemental distribution was analyzed by TEM-energy dispersive spectroscopy (TEM-EDS). For TEM imaging, the nanoparticles were dispersed in ultrapure water and briefly sonicated to ensure a homogeneous dispersion, which was then slowly dropped onto a copper grid. The grid was allowed to dry before observation.

Characterization of Membrane-Liposome Fusion

For the FRET assay, the cell membrane was pre-labeled with DiO/DiI dye pair, after which liposome-encapsulated nanoparticles were added. The mixture was subjected to ultrasonication for 15 min to promote membrane fusion. Fluorescence spectra were recorded before and after ultrasonication, so as to monitor the changes in fluorescence peaks.

Characterization of MSA-2 Encapsulation Efficiency

The encapsulation efficiency of MSA-2 was characterized by high-performance liquid chromatography (HPLC). Chromatographic separation was performed using a binary mobile-phase system consisting of A: 0.03% H_3PO_4 and B: acetonitrile (ACN), operated under gradient elution as follows: 0–2 min, 10% B; 2–7 min, linear increase to 90% B; 7–12 min, 90% B; 12.0–12.2 min, return to 10% B; 12.2–15 min, 10% B for re-equilibration. A 150 mm × 4.6 mm, 5 μm column was used at a flow rate of 1 mL/min. Analyte detection was achieved by UV absorbance at 325 nm.

Characterization of the Gene Loading and Protection Capacities of Carriers

To indirectly quantify the encapsulation efficiency (EE), siRNA was labeled with Cy5. The procedure was as follows: First, a series of Cy5-siRNA standard solutions with concentration gradients were prepared. The fluorescence intensity was measured at an excitation wavelength of 649 nm and an emission wavelength of 670 nm. A standard curve was plotted with concentration as the abscissa and fluorescence intensity as the ordinate, and a linear equation was fitted. A precise volume of the Cy5-siRNA solution was transferred to measure its fluorescence intensity (denoted as F_0), and the total siRNA content (W_0) was calculated based on the standard curve. The prepared Cy5-siRNA nanoparticle suspension was added to an ultrafiltration centrifuge tube with the corresponding molecular weight cut-off. After centrifugation at 12,000 × g, the filtrate was collected. The fluorescence intensity of the filtrate was measured (denoted as F_1), and the free siRNA content (W_1) was calculated. The encapsulation efficiency (EE) was calculated according to the formula: $EE\ (\%) = [(W_0 - W_1) / W_0] \times 100\% = [(F_0 - F_1) / F_0] \times 100\%$. At least three parallel samples were set for the experiment, and the results are expressed as $\bar{x} \pm s$.

Agarose gel electrophoresis was employed to assess nucleic-acid protection. Free siRNA and carrier-encapsulated siRNA were co-incubated with RNase at 37℃. At 0, 2, 4 and 6 h, proteinase K was added to terminate the RNase reaction. GelRed nucleic acid dye was then added, and the samples were loaded into solidified agarose gel. Electrophoresis was performed at 100 V for 30 min. After electrophoresis, the agarose gel was visualized in a gel imaging system.

Characterization of EZ/MS Ex Vivo Release

To assess pH-dependent release, the prepared nanoparticle suspension was equally divided into nine aliquots (500 μL each), and transferred into nine centrifuge tubes. Each tube was supplemented with

5 mL of 0.2 mol/L HEPES buffer (pH 4.5, 6.0, or 7.4, n = 3 per pH). At specific time points (0, 2, 4, 6, 24, and 48 h), 500 μL of the suspension was withdrawn from each tube and subjected to ultrafiltration, and the filtrate was collected. An equal volume of dissolution medium was then added to the filtrate. The filtrate was analyzed by ultraviolet spectrophotometry with a full-wavelength scan from 200 nm to 800 nm, and the absorbance at the characteristic absorption peak (270 nm) of EGCG was recorded.

MTT assay

GL261 cells were incubated with formulations at various concentrations for 48 h. After removing the drug-containing medium, MTT working solution was added, followed by a further 4 h incubation. The supernatant was then discarded, 150 μL DMSO was added to each well, and the formazan crystals were dissolved on a shaker for 5 min. The absorbance at 570 nm was measured using a microplate reader, and cell viability was calculated accordingly.

Determination of Cellular Uptake and Lysosomal Escape

GL261 and HCMEC/D_3 cells were co-cultured with Cy5-labeled formulations for a designated period. After removal of the drugs and washing, nuclei were stained with Hoechst 33342, and lysosomes were stained with LysoTracker Green. The samples were observed using confocal microscopy.

Ex Vivo Transwell Assay

HCMEC/D_3 cells were pre-cultured in the upper chamber until the transepithelial electrical resistance (TEER) reached 100 $\Omega \cdot cm^{2,}$ indicating establishment of a confluent barrier monolayer. GL261 cells were seeded in the lower chamber. Cy5-labeled nanoparticles were added to the upper chamber, and the co-culture was maintained for 24 h. The fluorescence intensity of GL261 cells was quantitatively measured using flow cytometry.

Western blot assay

GL261 cells were co-cultured with the formulations for 6 h. The drug-containing medium was discarded and replaced with complete medium for continued incubation. Cells were lysed using RIPA lysis buffer to extract proteins, and protein concentration was determined using a BCA protein assay kit (Thermo Fisher Scientific, USA). Equal amounts of protein were loaded and separated by sodium dodecyl sulfate-polyacrylamide gradient gel electrophoresis (SDS-PAGE). The proteins were then transferred onto a polyvinylidene fluoride (PVDF) membrane. The membranes were incubated overnight at 4℃ with primary antibodies (anti-IRF3 antibody, anti-phospho-IRF3 antibody, anti-TBK1 antibody, anti-phospho-TBK1 antibody, anti-IFN-β antibody), followed by incubation with an HRP-conjugated goat anti-rabbit IgG secondary antibody was added. Protein bands were detected using enhanced chemiluminescence.

RNA extraction and RT-qPCR

Cells were incubated with the formulations for 6 h. Subsequently, the drug-containing medium was removed and replaced with complete medium, and the culture was continued for an additional 48 h. Total RNA was extracted using Trizol reagent. cDNA synthesis was performed using the High-Capacity RNA-to-cDNA™ Kit (Applied Biosystems, USA). Quantitative PCR (qPCR) was conducted using SYBR Green Premix PCR reagent on a Real-Time PCR System 7500 instrument. GAPDH was used as the internal reference.

Elisa assay

Cell culture supernatants were collected after centrifugation at 4°C and 10,000 g for 10 min. Serum samples were obtained from animals. The levels of IFN-β, IL-6, Tumor Necrosis Factor-α (TNF-α), methionine, alanine aminotransferase (ALT), aspartate aminotransferase (AST), alkaline phosphatase (ALP), blood urea nitrogen (BUN), triglycerides (TG), uric acid (UA), and lactate dehydrogenase (LDH) were determined strictly in accordance with the manufacturer's instructions.

In Vitro Assays for GL261 and CTLL-2 Activity Detection

After a 6-hour pretreatment of the tumor cells with the formulations, they were seeded in the lower chamber of a transwell system, whereas CTLL-2 cells were seeded in the upper chamber. The co-culture was maintained in a medium containing 30 μM methionine. The cells were stained with Annexin V/Propidium Iodide (Annexin V/PI), and cell viability was assessed by flow cytometry.

In Vivo Antitumor Effects and Immunological Mechanisms of Ectopic Glioma

GL261 cells were harvested by trypsinization, pelleted by centrifugation, and resuspended in serum-free medium. The cell concentration was adjusted to 1×10^7 cells/mL using a cell counter. 100 μL of the cell suspension was injected subcutaneously into the right dorsal flank of the mice.

In Vivo Antitumor Effects/Immunological Mechanisms of In Orthotopic Glioma

GL261-luc cells were treated as the GL261 cells. Cell concentration was adjusted to 1×10^5 cells/μL using a cell counter. A volume of 5 μL of the cell suspension was used for tumor inoculation. The injection site was located 1 mm posterior to the bregma, 2 mm lateral to the sagittal suture (right side), and 2 mm beneath the dura mater.

Flow Cytometric Analysis of Tumor Tissues In Vivo

Tumor-bearing mice were euthanized by cervical dislocation. Following disinfection with 75% ethanol, tumor tissues were aseptically dissected, rinsed with PBS to remove necrotic tissue and fascia, and minced into 1–2 mm^3 pieces. The minced tissue was digested with pre-warmed digestion buffer (containing 1–2 mg/mL collagenase IV, 0.1–0.2 mg/mL hyaluronidase, and 20–50 μg/mL DNase I) on a shaker at 37°C for 30–60 min. The enzymatic reaction was terminated by adding RPMI-1640 medium supplemented with 10% FBS. The resulting cell suspension was filtered through a 70 μm cell strainer and centrifuged at 500 × g for 5 min at 4°C. The cell pellet was treated with ACK red blood cell lysis buffer at room temperature for 3–5 min, washed with PBS, and resuspended to obtain a single-cell suspension.

Single-cell suspensions (1×10^6 cells) were centrifuged at 500 g for 5 min at 4°C and resuspended in a blocking buffer containing 10% FBS to block Fc receptors, followed by incubation at 4°C for 15 min. A cocktail of the following fluorochrome-conjugated antibodies was added simultaneously: PE-Cy7-anti-I-A/I-E, APC-anti-CD11c, BV510-anti-CD45, PerCP-cy5.5-anti-CD3e and APC-cy7-anti-CD8a (final antibody concentrations were adjusted according to the manufacturer's instructions). The cells were incubated with the antibody mixture at 4°C in the dark for 30 min. After incubation, the cells were washed twice with PBS (centrifugation at 500 g for 5 min at 4°C) and resuspended in 300 μL of PBS.

After pre-warming and calibration, the flow cytometer was used for sample acquisition with the following gating strategy: Total immune cells were gated as the $CD45^+$ cell population; Mature dendritic cells (DCs) were identified as the $CD45^+I\text{-}A/I\text{-}E^+CD11c^+$ cell population; $CD8^+$ T cells were defined as the $CD45^+CD3^+CD8^+$ cell population. The percentages of each cell subset and the expression levels of target molecules were quantified.

Immunofluorescence Determination of Intratumoral Tissues in Vivo

Tumor tissues were harvested, fixed in paraformaldehyde, embedded

in paraffin, and sectioned. After deparaffinization, rehydration, and antigen retrieval via microwave treatment in citrate buffer, sections were blocked with BSA. A mixture of primary antibodies anti-CD45, anti-SLC43A2, anti-CD3, and anti-CD8 was applied and incubated overnight at 4℃. Following PBS washes, fluorescent secondary antibodies were incubated in the dark. Nuclei were counterstained with DAPI, and the sections were mounted for observation under a confocal microscope.

In Vivo Biosafety Determination

Female C57BL/6 J mice were administered the indicated formulations. Peripheral blood was collected from the retro-orbital venous plexus on days 7 and 14 post-administration. The samples were centrifuged at 3000 rpm for 15 min at 4℃. The upper pale-yellow, clear serum layer was aspirated. Serum levels of alanine aminotransferase (ALT), aspartate aminotransferase (AST), alkaline phosphatase (ALP), blood urea nitrogen (BUN), triglycerides (TG), uric acid (UA), and lactate dehydrogenase (LDH) were measured using commercial assay kits.

The fixed tissue blocks were dehydrated, embedded in paraffin to create wax blocks, and sectioned. The sections were then subjected to dewaxing, hematoxylin and eosin (H&E) staining, dehydration, clearing, and mounting to produce pathological slides suitable for microscopic observation.

Statistical Analysis

All experimental results were obtained from at least three independent replicate experiments, and the data were expressed as mean ± standard deviation. GraphPad software was used to perform intergroup difference analysis via one-way analysis of variance (one-way ANOVA). Statistical significance was indicated as follows: *P < 0.05; **P < 0.01, ***P < 0.001, **** P < 0.0001.

CRediT authorship contribution statement

Ran Huo: Conceptualization. **Yitong Liu:** Methodology, Investigation. **Chunying Cui:** Visualization, Supervision, Funding acquisition. **Dong Mei:** Methodology, Investigation. **Shuang Zhang:** Visualization, Validation, Supervision, Formal analysis, Data curation. **Yan Su:** Methodology, Investigation. **Yaoqi Wang:** Visualization, Validation, Supervision, Formal analysis. **Wentao Zhang:** Methodology, Investigation. **Muhan Zhang:** Investigation. **Chunyu Zhao:** Validation, Data curation. **Shuxin Luo:** Investigation. **Qi Sun:** Supervision, Methodology, Investigation. **Yingdong Ma:** Validation. **Chang Na:** Validation, Data curation, Conceptualization. **Jingyi Ye:** Validation. **Yang Tian:** Writing – review & editing, Writing – original draft, Methodology, Formal analysis, Conceptualization. **Yadong Xing:** Conceptualization. **Siyu Liu:** Conceptualization.

Declaration of Competing Interest

The authors declare that they have no known competing financial interests or personal relationships that could have appeared to influence the work reported in this paper.

Acknowledgments

This work was supported by the National Natural Science Foundation of China (81502688, 8240130907, 82304390) and a grant (CX25YZ02) from the Chinese Institutes for Medical Research, Beijing. Cooperation Research Funding of Capital Medical University (2020KJ000514), Cooperation Research Funding of Capital Medical University (2023KJ000814), R&D Program of Beijing Municipal Education Commission (KM202210025024).

Appendix A. Supporting information

Supplementary data associated with this article can be found in the online version at doi:10.1016/j.nantod.2026.103061.

Data availability

Data will be made available on request.

References

[1] G. Castellani, T. Croese, J.M. Peralta Ramos, et al., Transforming the understanding of brain immunity [J], Science 380 (6640) (2023) eabo7649.
[2] M. Qian, G. Jiang, S. Zhao, et al., Modulating nano-bio interface via drug-framework hybridization to activate chemoimmunotherapy against glioma postoperative recurrence [J], Cell Biomater. 1 (3) (2025) 100025.
[3] M.D. Sweeney, A.P. Sagare, B.V. Zlokovic, Blood-brain barrier breakdown in Alzheimer disease and other neurodegenerative disorders [J], Nat. Rev. Neurol. 14 (3) (2018) 133–150.
[4] E.K. Nduom, M. Weller, A.B. Heimberger, Immunosuppressive mechanisms in glioblastoma [J], Neuro Oncol. 17 (7) (2015) vii9–vii14. Suppl 7.
[5] K. Woroniecka, P. Chongsathidkiet, K. Rhodin, et al., T-Cell Exhaustion Signatures Vary with Tumor Type and Are Severe in Glioblastoma [J], Clin. Cancer Res 24 (17) (2018) 4175–4186.
[6] P. Chongsathidkiet, C. Jackson, S. Koyama, et al., Sequestration of T cells in bone marrow in the setting of glioblastoma and other intracranial tumors [J], Nat. Med 24 (9) (2018) 1459–1468.
[7] B.S. Pan, S.A. Perera, J.A. Piesvaux, et al., An orally available non-nucleotide STING agonist with antitumor activity [J], Science 369 (6506) (2020) eaba6098.
[8] J. Yang, Z. Luo, J. Ma, et al., A next-generation STING agonist MSA-2: From mechanism to application [J], J. Control Release 371 (2024) 273–287.
[9] Y. Chen, L. Liu, Modern methods for delivery of drugs across the blood-brain barrier [J], Adv. Drug Deliv. Rev. 64 (7) (2012) 640–665.
[10] J. Liu, C. Liu, Y. Ma, et al., STING inhibitors sensitize platinum chemotherapy in ovarian cancer by inhibiting the CGAS-STING pathway in cancer-associated fibroblasts (CAFs) [J], Cancer Lett. 588 (2024) 216700.
[11] J. Zheng, J. Mo, T. Zhu, et al., Comprehensive elaboration of the cGAS-STING signaling axis in cancer development and immunotherapy [J], Mol. Cancer 19 (1) (2020) 133.
[12] Y. Bian, W. Li, D.M. Kremer, et al., Cancer SLC43A2 alters T cell methionine metabolism and histone methylation [J], Nature 585 (7824) (2020) 277–282.
[13] M. Pandit, Y.S. Kil, J.H. Ahn, et al., Methionine consumption by cancer cells drives a progressive upregulation of PD-1 expression in CD4 T cells [J], Nat. Commun. 14 (1) (2023) 2593.
[14] T. Li, Y.T. Tan, Y.X. Chen, et al., Methionine deficiency facilitates antitumour immunity by altering m(6)A methylation of immune checkpoint transcripts [J], Gut 72 (3) (2023) 501–511.
[15] N. Yang, Y. Yan, Z. Li, et al., Nintedanib-amplified effects of HSP47 siRNA on liver fibrosis therapy by inhibiting collagen secretion [J], J. Control Release 388 (Pt 2) (2025) 114378.
[16] I. Hwang, H. Uchida, Z. Dai, et al., Cellular stress signaling activates type-I IFN response through FOXO3-regulated lamin posttranslational modification [J], Nat. Commun. 12 (1) (2021) 640.
[17] A. El-Kenawi, A. Berglund, V. Estrella, et al., Elevated Methionine Flux Drives Pyroptosis Evasion in Persister Cancer Cells [J], Cancer Res 83 (5) (2023) 720–734.
[18] Y.-Q. Xu, P. Yu, W. Zhou, Combined effect of pH and temperature on the stability and antioxidant capacity of epigallocatechin gallate (EGCG) in aqueous system [J], J. Food Eng. 250 (2019) 46–54.
[19] G. Lu, X. Wang, F. Li, et al., Engineered biomimetic nanoparticles achieve targeted delivery and efficient metabolism-based synergistic therapy against glioblastoma [J], Nat. Commun. 13 (1) (2022) 4214.
[20] Y. Zou, Y. Wang, S. Xu, et al., Brain Co-Delivery of Temozolomide and Cisplatin for Combinatorial Glioblastoma Chemotherapy [J], Adv. Mater. 34 (33) (2022) e2203958.
[21] G. Morad, C.V. Carman, E.J. Hagedorn, et al., Tumor-Derived Extracellular Vesicles Breach the Intact Blood–Brain Barrier via Transcytosis [J], ACS Nano 13 (12) (2019) 13853–13865.
[22] S. Chi, L. Zhang, H. Cheng, et al., Biomimetic Nanocomposites Camouflaged with Hybrid Cell Membranes for Accurate Therapy of Early-Stage Glioma [J], Angew. Chem. Int Ed. Engl. 62 (29) (2023) e202304419.
[23] L. Wang, S. Quine, A.N. Frickenstein, et al., Exploring and Analyzing the Systemic Delivery Barriers for Nanoparticles [J], Adv. Funct. Mater. 34 (8) (2024) 2308446.
[24] J. Li, X. Gao, Y. Wang, et al., Precision design of engineered nanomaterials to guide immune systems for disease treatment [J], Matter 5 (4) (2022) 1162–1191.
[25] H. Nie, R. Huang, G. Jiang, et al., Modulating active targeting nanoparticle design according to tumor progressions [J], Acta Pharm. Sin. B 15 (2) (2025) 1143–1158.
[26] W.B. Zhang, Z. Wang, F. Shu, et al., Activation of AMP-activated protein kinase by temozolomide contributes to apoptosis in glioblastoma cells via p53 activation and mTORC1 inhibition [J], J. Biol. Chem. 285 (52) (2010) 40461–40471.
[27] Y. Ma, Y. Vassetzky, S. Dokudovskaya, mTORC1 pathway in DNA damage response [J], Biochimica et Biophysica Acta (BBA) - Molecular Cell Research 1865 (9) (2018) 1293–1311.

[28] M. Shimobayashi, M.N. Hall, Multiple amino acid sensing inputs to mTORC1 [J], Cell Res 26 (1) (2016) 7–20.
[29] P. Nicklin, P. Bergman, B. Zhang, et al., Bidirectional transport of amino acids regulates mTOR and autophagy [J], Cell 136 (3) (2009) 521–534.
[30] D. Lamoral-Theys, M. Le Mercier, B. Le Calvé, et al., Long-term temozolomide treatment induces marked amino metabolism modifications and an increase in TMZ sensitivity in Hs683 oligodendroglioma cells [J], Neoplasia 12 (1) (2010) 69–79.
[31] L.M. Coussens, Z. Werb, Inflammation and cancer [J], Nature 420 (6917) (2002) 860–867.
[32] D.W. Beury, K.H. Parker, M. Nyandjo, et al., Cross-talk among myeloid-derived suppressor cells, macrophages, and tumor cells impacts the inflammatory milieu of solid tumors [J], J. Leukoc. Biol. 96 (6) (2014) 1109–1118.
[33] M. Shen, X. Jiang, Q. Peng, et al., The cGAS-STING pathway in cancer immunity: mechanisms, challenges, and therapeutic implications [J], J. Hematol. Oncol. 18 (1) (2025) 40.
[34] X. Chen, L. Liu, S. Kang, et al., The lactate dehydrogenase (LDH) isoenzyme spectrum enables optimally controlling T cell glycolysis and differentiation [J], Sci. Adv. 9 (12) (2023) eadd9554.
[35] G. Claps, S. Faouzi, V. Quidville, et al., The multiple roles of LDH in cancer [J], Nat. Rev. Clin. Oncol. 19 (12) (2022) 749–762.
[36] V. Lala, M. Zubair, D.A. Minter, Liver Function Tests. StatPearls [Internet]. Treasure Island (FL), StatPearls Publishing, 2026.
[37] C. Chitraju, A.W. Fischer, Y.A. Ambaw, et al., Mice lacking triglyceride synthesis enzymes in adipose tissue are resistant to diet-induced obesity [J], Elife 12 (2023) RP88049.
[38] C. Wang, B. Wu, Y. Wu, et al., Camouflaging Nanoparticles with Brain Metastatic Tumor Cell Membranes: A New Strategy to Traverse Blood–Brain Barrier for Imaging and Therapy of Brain Tumors [J], Adv. Funct. Mater. 30 (14) (2020) 1909369.
[39] X. Tian, S. Nyberg, S.S. P, et al., LRP-1-mediated intracellular antibody delivery to the Central Nervous System [J], Sci. Rep. 5 (2015) 11990.
[40] S. Habib, M. Singh, Angiopep-2-Modified Nanoparticles for Brain-Directed Delivery of Therapeutics: A Review [J], Polym. (Basel) 14 (4) (2022) 712.
[41] W. Zhang, A. Refaat, H. Li, et al., Optimizing Angiopep-2 Density on Polymeric Nanoparticles for Enhanced Blood–Brain Barrier Penetration and Glioblastoma Targeting: Insights From In Vitro and In Vivo Experiments [J], Adv. Funct. Mater. 35 (38) (2025) 2425165.
[42] M. Demeule, J.C. Currie, Y. Bertrand, et al., Involvement of the low-density lipoprotein receptor-related protein in the transcytosis of the brain delivery vector angiopep-2 [J], J. Neurochem. 106 (4) (2008) 1534–1544.
[43] H. Sun, J. Su, Q. Meng, et al., Cancer-Cell-Biomimetic Nanoparticles for Targeted Therapy of Homotypic Tumors [J], Adv. Mater. 28 (43) (2016) 9581–9588.
[44] X. Zhu, Z. Shi, Y. Mao, et al., Cell Membrane Perforation: Patterns, Mechanisms and Functions [J], Small 20 (24) (2024) e2310605.
[45] X. Duan, Y. Zhang, M. Guo, et al., Sodium alginate coating simultaneously increases the biosafety and immunotherapeutic activity of the cationic mRNA nanovaccine [J], Acta Pharm. Sin. B 13 (3) (2023) 942–954.
[46] S. Rayamajhi, J. Marchitto, T.D.T. Nguyen, et al., pH-responsive cationic liposome for endosomal escape mediated drug delivery [J], Colloids Surf. B Biointerfaces 188 (2020) 110804.
[47] P. Wu, H. Zhang, Y. Yin, et al., Engineered EGCG-Containing Biomimetic Nanoassemblies as Effective Delivery Platform for Enhanced Cancer Therapy [J], Adv. Sci. (Weinh.) 9 (15) (2022) e2105894.
[48] M. Qin, Z. Feng, H. Meng, Targeting metalloimmunology via a nanoenabled approach to effectively treating solid tumors [J], Chem 10 (4) (2024) 1041–1043.
[49] N. Yang, J. Yang, Y. Liu, et al., Impaired learning and memory in mice induced by nano neodymium oxide and possible mechanisms [J], Environ. Toxicol. 36 (8) (2021) 1514–1520.
[50] N. Yang, F. Chen, J. Yang, et al., Comprehensive Review on the Toxicology of Neodymium Oxide and Pharmaceutical Applications [J], J. Appl. Toxicol. 45 (11) (2025) 2257–2264.